© 2015. Published by The Company of Biologists Ltd | Development (2015) 142, 4158-4167 doi:10.1242/dev.127019

TECHNIQUES AND RESOURCES

RESEARCH ARTICLE

Simultaneous imaging of blood flow dynamics and vascular remodelling during development

Siavash Ghaffari[1,2], Richard L. Leask[2] and Elizabeth A. V. Jones[1,2,3,*]

ABSTRACT

Normal vascular development requires blood flow. Time-lapse imaging techniques have revolutionised our understanding of developmental biology, but measuring changes in blood flow dynamics has met with limited success. Ultrasound biomicroscopy and optical coherence tomography can concurrently image vascular structure and blood flow velocity, but these techniques lack the resolution to accurately calculate fluid forces such as shear stress. This is important because hemodynamic forces are biologically active and induce changes in the expression of genes important for vascular development. Regional variations in shear stress, rather than the overall level, control processes such as vessel enlargement and regression during vascular remodelling. We present a technique to concurrently visualise vascular remodelling and blood flow dynamics. We use an avian embryonic model and inject an endothelial-specific dye and fluorescent microspheres. The motion of the microspheres is captured with a high-speed camera and the velocity of the blood flow in and out of the region of interest is quantified by micro-particle image velocitymetry (μPIV). The vessel geometry and flow are used to numerically solve the flow physics with computational fluid dynamics (CFD). Using this technique, we can analyse changes in shear stress, pressure drops and blood flow velocities over a period of 10 to 16 h. We apply this to study the relationship between shear stress and chronic changes in vessel diameter during embryonic development, both in normal development and after TGFβ stimulation. This technique allows us to study the interaction of biomolecular and biomechanical signals during vascular remodelling using an *in vivo* developmental model.

KEY WORDS: Angiogenesis, Arteriogenesis, Hemodynamics, Time-lapse microscopy, Micro-particle image velocimetry, Computational fluid dynamics

INTRODUCTION

Vascular remodelling is an essential component of vascular development. The first vessels that form during development arise before the onset of blood flow and form a honeycomb-shaped network called the capillary plexus. With the onset of flow, this early vascular network is remodelled into morphologically distinct arteries and veins. Blood flow is essential for vascular remodelling during development. If normal blood flow is not present, then remodelling does not occur (Chapman, 1918; Lucitti et al., 2007; Wakimoto et al., 2000). Remodelling involves angiogenesis, the formation of new vessels, and arteriogenesis, the enlargement of existing vessels. Blood flow creates mechanical forces on the endothelium, and endothelial cells are able to sense these forces and alter their gene expression (Abe and Berk, 2014; Bryan et al., 2014; Jones, 2011). The dependence of remodelling on blood flow is well established, yet there is a lack of understanding of the basic mechanisms by which remodelling occurs.

One of the greatest difficulties in understanding the interplay of flow dynamics and vascular development is that few tools exist to study flow dynamics in real time *in vivo*. During development, the geometry of the vascular network and flow rate change significantly. Clinical imaging and numerical simulations have been used to study the flow dynamics in developed vessels (Gijsen et al., 2007; Mantha et al., 2006; Robles et al., 2015; Steinman et al., 2003). However, these techniques are unsuitable to study microscopic processes during remodelling, which requires a resolution of at least 1 μm. As such, no method currently offers the ability to study the movement of endothelial cells concurrently with an analysis of the evolving flow dynamics during remodelling.

Blood flow in the early embryo is characterised as Stokes flow, which occurs when the viscous forces are much larger than the inertial forces (i.e. the forces resulting from the momentum of the fluid). Average embryonic blood velocity is relatively slow (often less than 1 mm/s, even during systole), providing little momentum, and the viscous forces in blood therefore dominate the flow physics (Jones et al., 2004). Stokes flow allows the partial differential equations that describe fluid momentum to be linearised. As such, the embryonic vasculature is an ideal one in which to study the interaction of flow dynamics and the endothelium, as compared to the adult where flow separation, turbulence and other complex fluid phenomena are present.

Though the calculation of flow patterns within embryonic vessels is relatively simple, the geometry of the vascular network is complex and constantly changing during development. Many studies on shear stress have relied on the assumption that increased flow rates result in increased shear stress (Milkiewicz et al., 2001; Ziada et al., 1989). Though this is a valid assumption for straight, unbranched blood vessels, shear stress levels cannot be calculated purely based on the flow rate for more complex geometries (Manbachi et al., 2011). In these more complicated situations, calculation of shear stress levels requires solving a set of partial differential equations, called the Navier–Stoke's equation, for each specific geometry.

In this work, we report a technique to simultaneously image blood flow dynamics and vascular development. We use a combination of time-lapse imaging, flow visualisation and computational fluid dynamics (CFD). The flow visualisation allows us to make localised measurements of the blood velocity at set time points and locations in the embryonic vasculature. The computational technique allows us to extend these measurements to

[1]Lady Davis Institute for Medical Research, McGill University, 3755 Chemin de la Côte-Ste-Catherine, Montréal, Quebec H3T 1E2, Canada. [2]Department of Chemical Engineering, McGill University, 3610 University Street, Montréal, Quebec H3A 0C5, Canada. [3]Department of Cardiovascular Science, KU Leuven, UZ Herestraat 49, Box 911, Leuven 3000, Belgium.

*Author for correspondence (liz.jones@med.kuleuven.be)

Received 1 June 2015; Accepted 17 September 2015

Development (2015) 142, 4158-4167 doi:10.1242/dev.127019

acquire the blood velocity in the entire region of interest, as well as allowing us to calculate other hemodynamic parameters such as the pressure drop, the vorticity and the shear stress. This allows us to follow the evolution of flow dynamics in real time as the vasculature remodels.

RESULTS

Imaging blood flow and vascular development by time-lapse microscopy

Evaluation of blood flow dynamics during vascular development requires a method to track both the changes in vascular network morphology and the blood flow velocity repeatedly over an extended period of time. Avian embryos were the model of choice because of the relatively low photo-sensitivity and flat geometry of the avian capillary plexus during development. We previously established a technique to time-lapse vascular development in avian embryos (Al-Roubaie et al., 2012). We cultured the embryos *ex ovo* and labelled the endothelial cells by intra-vascular injection of fluorescently labelled acetylated low-density lipoprotein (AF488-AcLDL) and used micro-particle image velocimetry (μPIV) to image the flow dynamics. This is done by intra-vascularly injecting fluorescent microspheres that act as tracers of the fluid motion and imaging the region of interest with a high-speed camera. To extract the velocity measurements from this data, the images of microsphere motion are divided into interrogation windows and the cluster of particles within each interrogation window is identified from frame-to-frame using a statistical cross-correlation (for review, see Adrian, 1991).

We analysed embryos at the stage where blood flow initiates [Hamburger Hamilton (HH)11 or 30 h of incubation], as this allowed us to study the process of vascular remodelling. We imaged the vascular network every 15 min using a high-resolution camera (Zeiss Axiocam, green in Movie 5). We followed the motion of the tracer particles using a high-speed camera that had high light sensitivity and could therefore capture fluorescence (FASTCAM Ultima APX-RS, red in Movie 5). The motion of the tracer particles was imaged once every 2 h for two entire cardiac cycles at 250 frames per second. The vasculature was imaged less frequently than the blood vessels to reduce phototoxic effects.

The original PIV technique was developed using laser-sheet illumination of the fluid motion to obtain a two-dimensional image of the tracer particle motion. Micro-PIV, however, is performed using a fluorescence microscope and results in the illumination of a three-dimensional space rather than a two-dimensional sheet. When blood flows within a vessel, the slowest motion is present next to the walls and the fastest motion is present in the centre of the vessel. Because of this, flow above and below the centreline is much slower than the flow in the centre of the vessel. Various post-processing techniques have been developed for μPIV to minimise the error associated with imaging a three-dimensional volume. Out-of-focus objects are larger in size and lower in fluorescence. Thus, either selection based on particle size or thresholding based on fluorescent intensity can be used to reject out-of-focus particles (Meinhart et al., 2000). Using flow channels with simple geometries where a theoretical solution to the blood flow profile was possible, Pitts et al. investigated the efficacy of these post-processing techniques (Pitts et al., 2012). They found that most common post-processing techniques for μPIV resulted in shear rate measurements that had as much as a four-fold error. We attempted to use μPIV for the entire region of interest and found that the technique could accurately measure velocities within straight vessel segments, but that, even with post-processing, shear rate measurements were inaccurate. For this reason, we limited our μPIV measurements to assess the velocity in straight vessel segments and then used this as an input to our computational solver to obtain the flow within the network. μPIV can be performed using open source software (i.e. OpenPIV, PIVLab, JPIV) or by developing one's own code, as we did.

The selection of an appropriate tracer particle is of paramount importance in μPIV. Particles must be neutrally buoyant, must not disturb the flow, and must be large enough to be unaffected by Brownian motion (Santiago et al., 1998). We investigated the use of several different types of fluorescent particles (polystyrene microspheres, liposomes, etc.). Though all the particle types tested met the criteria for μPIV, they all suffered from one important limitation: in all cases, the particles adhered to the luminal side of the vessel wall within 2-3 h of injection. Polyethylene glycol (PEG) is often used to make 'stealth' micro-particles in biological applications (Immordino et al., 2006). PEG is highly hydrophobic and creates a shell of water around PEGylated surfaces. To covalently link PEG to the microsphere surface, we used carboxy-modified polystyrene microspheres and amino 5 K PEG. We followed the manufacturer's protocol for covalent coupling of proteins to the carboxy-modified polystyrene microsphere. After PEGylation, we found that the microspheres circulated for ∼16 h. Particles did gradually adhere to the vessel wall, but a large number of particles were still circulating at the end of the time-lapse.

Because blood velocity measurements were less frequent than images of the vascular network, we needed a method to interpolate between velocity measurement time points. Flow was imaged for two cardiac cycles at each time point, and the velocity of the blood flow during the cardiac cycle was extracted (Fig. 1A). To obtain

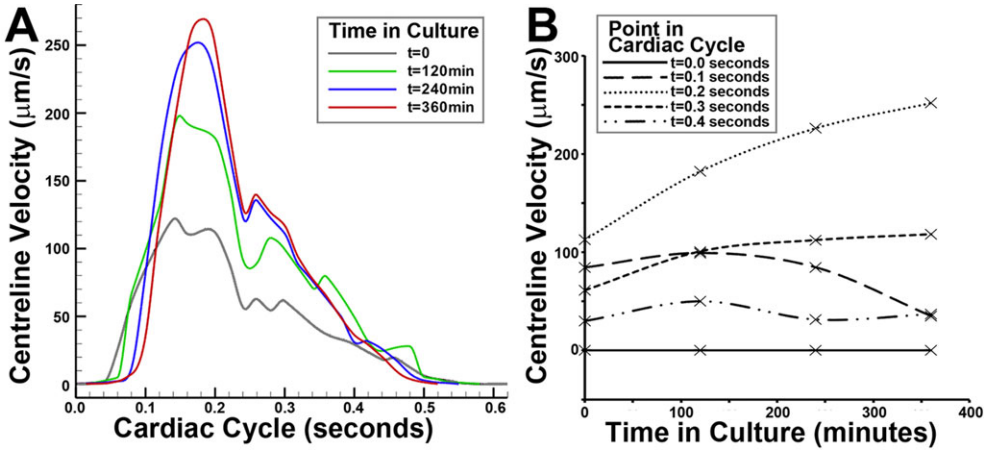

Fig. 1. Analysis of changes in cardiac cycle during the time-lapse experiment. The blood flow velocity in the centre of the vessel was analysed for all inlet and outlet vessels to the region of interest using μPIV. A typical cardiac cycle for one vessel segment is shown taken at four time points within the time-lapse experiment (A). As the velocity was measured less frequently than the vascular morphology, it was necessary to interpolate between the velocity measurement time points. Interpolation was performed cross-plotting the data from the cardiac cycle and fitting a line to the velocity over the entire time-lapse at multiple points in the cardiac cycle (B).

Development (2015) 142, 4158-4167 doi:10.1242/dev.127019

flow information between flow measurement time points, an interpolation was made based on the trend of the velocity data at different points in the cardiac cycle for the entire time-lapse experiment (Fig. 1B). Only five points in the cardiac cycle are displayed in Fig. 1B for the sake of simplicity, however, additional points in the cardiac cycle were analysed depending on the specific experimental needs.

Viscosity estimates in embryonic vessels

Calculation of hemodynamic properties, such as the shear stress, requires an estimate of the viscosity of the fluid. Blood viscosity changes with haematocrit and with shear rate (i.e. the velocity gradient of the blood). Red blood cells form in the blood islands and enter circulation gradually with the onset of blood flow (Lucitti et al., 2007). Thus, the haematocrit is not constant during early vascular development. To measure changes in haematocrit with respect to embryonic stage, we injected embryos with fluorescent dextran and then isolated the whole embryo and placed it in culture on a heated confocal microscope. We used the line-scanning function of the confocal microscope to scan across one vessel repeatedly such that we obtained an x versus time image (Fig. 2A). In these images, the blood plasma is fluorescent from the dextran injection and the red blood cells appear as black streaks within the vessel. By evaluating the percentage of black pixels within the vessels, we could estimate the haematocrit of the blood.

In vessels smaller than 300 µm, the haematocrit is dependent on the vessel diameter as a result of a phenomenon called the Fahraeus effect (Fahraeus, 1929). We therefore measured the haematocrit with respect to diameter at different stages (Fig. 2B). We found that the data fit to a previously published equation for the Fahraeus effect in smaller vessels (Pries et al., 1990), such that:

$$\frac{H_T}{H_D} = H_D + (1 - H_D)\,(1 + 1.7e^{-0.35D} - 0.6e^{-0.01D}). \quad (1)$$

Where H_T is the tube haematocrit (i.e. the effective haematocrit in a small vessel), H_D is the discharge haematocrit (i.e. the constant haematocrit present in larger vessels and in the heart) and D is the diameter. As such, we used the haematocrit and the diameter from each measurement to calculate a discharge haematocrit for each stage. We then plotted the average discharge haematocrit with respect to somite stage (Fig. 2C). The data was fit to a cubic equation as a means to easily calculate the haematocrit in our computational analysis.

We previously published values for the viscosity of avian blood at different shear rates and haematocrits for embryos between 4 days and 6 days of incubation, or HH22 to HH34 (Al-Roubaie et al., 2011). Embryos used in this current work were much younger, starting at 30 h of incubation (13 somites or HH11). Ideally, we would have extended our previous work to younger stages; however, we were unable to collect enough blood to make viscosity measurements from embryos younger than HH22. We were therefore obliged to work with the data available. Most work on embryonic blood flow assumes that embryonic blood has the same properties as adult blood (Jones, 2011; Poelma et al., 2008). Thus, the use of data from embryonic blood, even from slightly older stages, represents an advance over previous estimates. Our previously published work indicated that the viscosity of embryonic blood fit a Carreau model, such that:

$$\mu = \mu_\infty + (\mu_0 - \mu_\infty)[1 + (\lambda\gamma)^2]^{\frac{N-1}{2}}. \quad (2)$$

Where the constants (μ_∞, μ_0, λ and N) are dependent on the stage of development and the haematocrit. γ is the shear rate. For each time point, we used the stage of development to establish H_D (based on Fig. 2C). We then used Eqn 1 to establish H_T for each vessel segment based on the average diameter of that segment. We evaluated the Carreau constants based on H_T and the stage of development by interpolating and extrapolating, respectively, from our previously published values for embryonic blood viscosity (Al-Roubaie et al., 2011). Because different vessel diameters are present within a region of interest, a different Carreau equation was applied to each vessel segment. This allows us to include shear rate-dependent effects on the viscosity in our computational analysis.

Calculating hemodynamic parameters

A stack of images comprising the image of the wall and the 500 high-speed images of the microsphere motion was flattened into a single image. The resultant image was filtered and thresholded to create a black and white image mask (see Fig. 3 for process, additional details in Materials and Methods). A Canny algorithm was applied to the image mask using the Matlab edge function to identify the inner wall boundaries of perfused vessels. The Canny

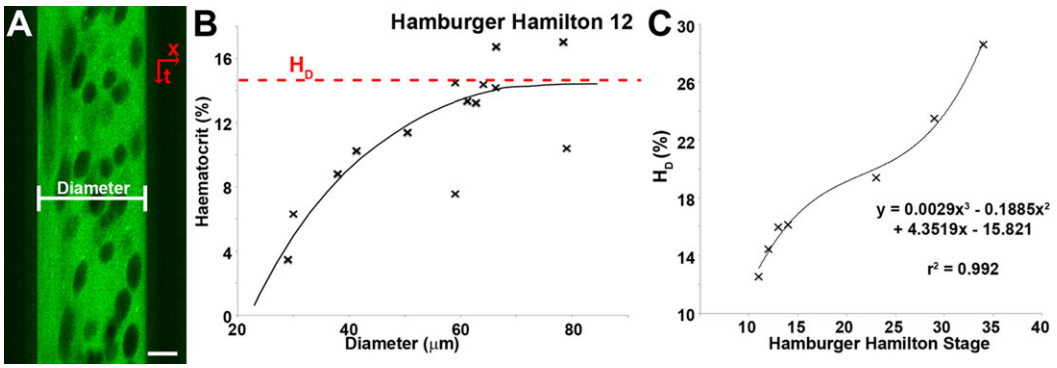

Fig. 2. Analysis of changes in haematocrit at different stages of development. (A) The haematocrit was analysed using a line scanning technique. Embryos were injected with fluorescent dextran, which labels the blood plasma, but is excluded from the red blood cells. The laser line was scanned at one location, perpendicular to the direction of blood flow, yielding an x versus time (t) image. The percentage of black pixels was used to estimate the haematocrit and the thickness of the green band to measure diameter. Scale bar: 20 µm. (B) The haematocrit was plotted with respect to the vessel diameter, and agreed with the equation for the Fahraeus effect (black line). Haematocrit measurements were normalised using the vessel diameter to calculate the effective discharge haematocrit (H_D, red dotted line). (C) The discharge haematocrit was measured at different stages (n=3-5 per stage). A cubic equation was fit to the data to allow it to be used in the computational analysis.

Development (2015) 142, 4158-4167 doi:10.1242/dev.127019

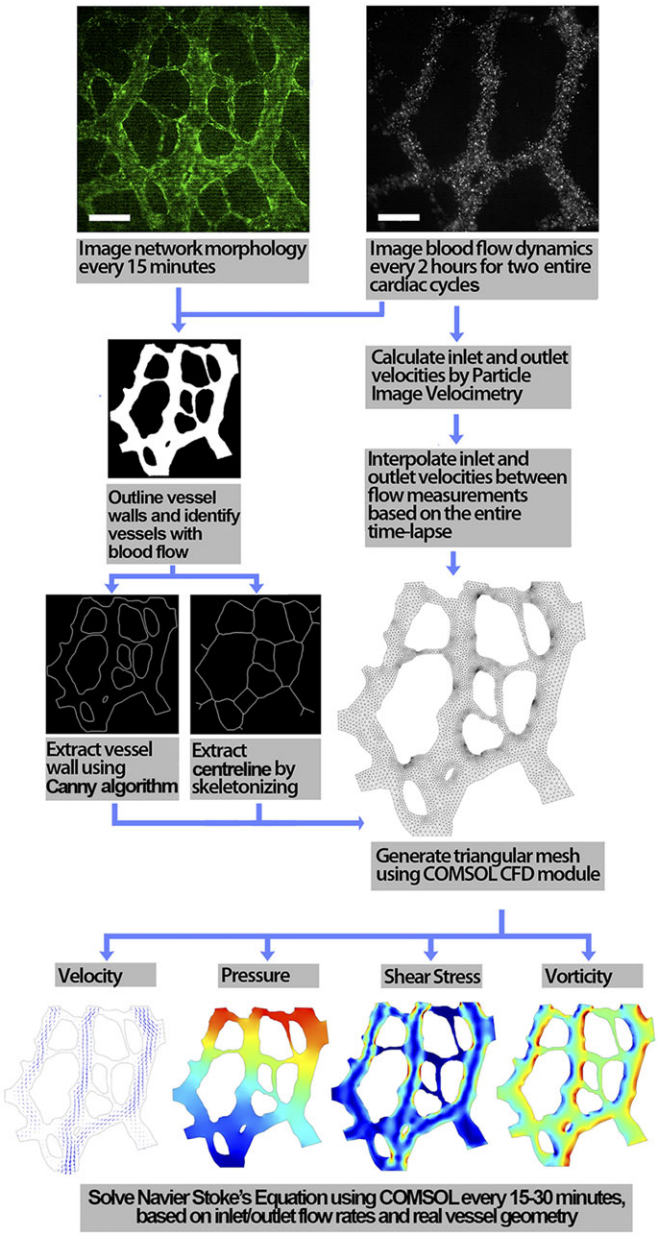

Fig. 3. Combination of time-lapse images and flow measurements using computational fluid dynamics. Images of endothelial cells labelled with Alexa Fluor488-acetylated low-density lipoprotein (AF488-AcLDL) were taken every 15 min for a period of 12-16 h. Fluorescent circulating microspheres were imaged every 2 h at 250 frames per second for 2 s. The set of 500 images of the microspheres and the image of the vessel wall were flattened and thresholded to produce an image mask. From the mask, the vessel outline and centreline were identified. Micro-particle image velocimetry (μPIV) was used on the microsphere images to quantify the inlet and outlet velocities. A CFD solver was used to generate a triangular mesh for the finite element analysis and from this fluid dynamic, parameters were calculated for the entire cardiac cycle at each time point. Scale bars: 200 μm.

method can produce equally thin edges with smooth continuous pixels even under noisy condition (Canny, 1986). The edge detection resulted in a matrix of black and white pixels that defined the location of the vessel walls. The mask was skeletonised to provide an image of only the centreline of the vessels. The distance between the centreline and the vessel wall was averaged for each segment, in order to define the vessel diameter for the viscosity estimates.

The vessel geometry, inlet and outlet flow rates to the region of interest and the viscosity estimates were then combined using a computational fluid dynamic (CFD) solver (Fig. 3). In the CFD solver (COMSOL Multiphysics), a 2D simulation was chosen. The solver was set to solve the flow for laminar, time-dependent, incompressible flow. As the vessel network has curved geometries, the numerical algorithm was applied on a non-orthogonal curvilinear coordinate framework. The solver uses a finite element model to solve the Navier–Stoke's equation. Mesh generation for the finite element model was done using the CFD solver and different mesh sizes were tested ('fine', 'extra-fine' and 'extremely fine'). The inlet and outlet boundary conditions were set using the measured flow rates for the cardiac cycle (Fig. 1). Inlet and outlet blood velocity measurements were made far from branch points, so fully developed flow was assumed at these points. Based on the Reynold's number of blood flow in embryonic vessels, the flow should become fully developed within a few microns of the branch points. For a network with N inlet and outlets, the velocities of $N-1$ segments were used as boundary conditions. For the last vessel segment, the pressure at the outlet was set to zero. Two convergence criteria were set in the solver: first, a mass flux residual of less than 10^{-8} for each control volume; second, $(|\phi_{i+1}-\phi_i|)/|\phi_{i+1}|\leq 10^{-10}$ for all time steps where ϕ represents v_x or v_y (flow velocities in x and y directions), and i is the number of iterations. This procedure was repeated for each time point in the time-lapse experiment.

The CFD solver outputs the velocity, shear stress, relative pressure and vorticity of the flow. The left panel of the movies shows the endothelial cell behaviour (Fig. 4A, Movies 1-3). The region outlined by the yellow box represents the region where flow was analysed. In this time-lapse, we observed both intussusceptive angiogenesis (cyan arrowhead, Movie 1) and sprouting angiogenesis (yellow arrow, Movie 1). Systolic velocities in the centre of the vessel were on the order of 500 μm/s at the beginning of the time-lapse (13 somites) and increased to ∼1500 μm/s 9 hours later, when embryos had reached 20 somites (Fig. 4B, Movie 1). These velocities are similar to those observed in vessels of the same diameter in the mouse embryo (Jones et al., 2004). We were also able to capture the first flow through newly lumenised blood vessels after angiogenesis (t=510 min for Movie 1). We calculated the relative pressure in the vessels (Fig. 4C, Movie 2) and found that the pressure drop was ∼1 Pa at early time points, but increased to 6 Pa by the end of the experiment. Wall shear stress at the start of the time-lapse was on average 0.064 Pa (n=3 embryos, s.e.m.=0.015) but increased to an average of 0.18 Pa (s.e.m.=0.02) by the end of the time-lapses (Fig. 4D, Movie 3). These shear stress measurements are of the same order of magnitude as previous shear stress estimates during early vascular development in mouse and avian embryos (Chouinard-Pelletier et al., 2013; Jones et al., 2004). Our computational model also allowed us to make the first estimates of vorticity in the remodelling embryonic vascular network (Fig. 4E, Movie 3). Vorticity is a measure of the angular velocity of the fluid. Despite the name, vorticity does not necessarily indicate the presence of a vortex. When an obstruction in the path of the flow is present, the fluid moves around the obstruction creating an angular component to the velocity vector. As such, vorticity can be used to identify bifurcations in the flow, which are biologically active regions in the vessel wall.

Validation of calculated flow rates

To validate our calculated hemodynamic profiles, we first investigated whether the method accurately predicted the pattern of blood flow at one single time point. We used images of flow from

Development (2015) 142, 4158-4167 doi:10.1242/dev.127019

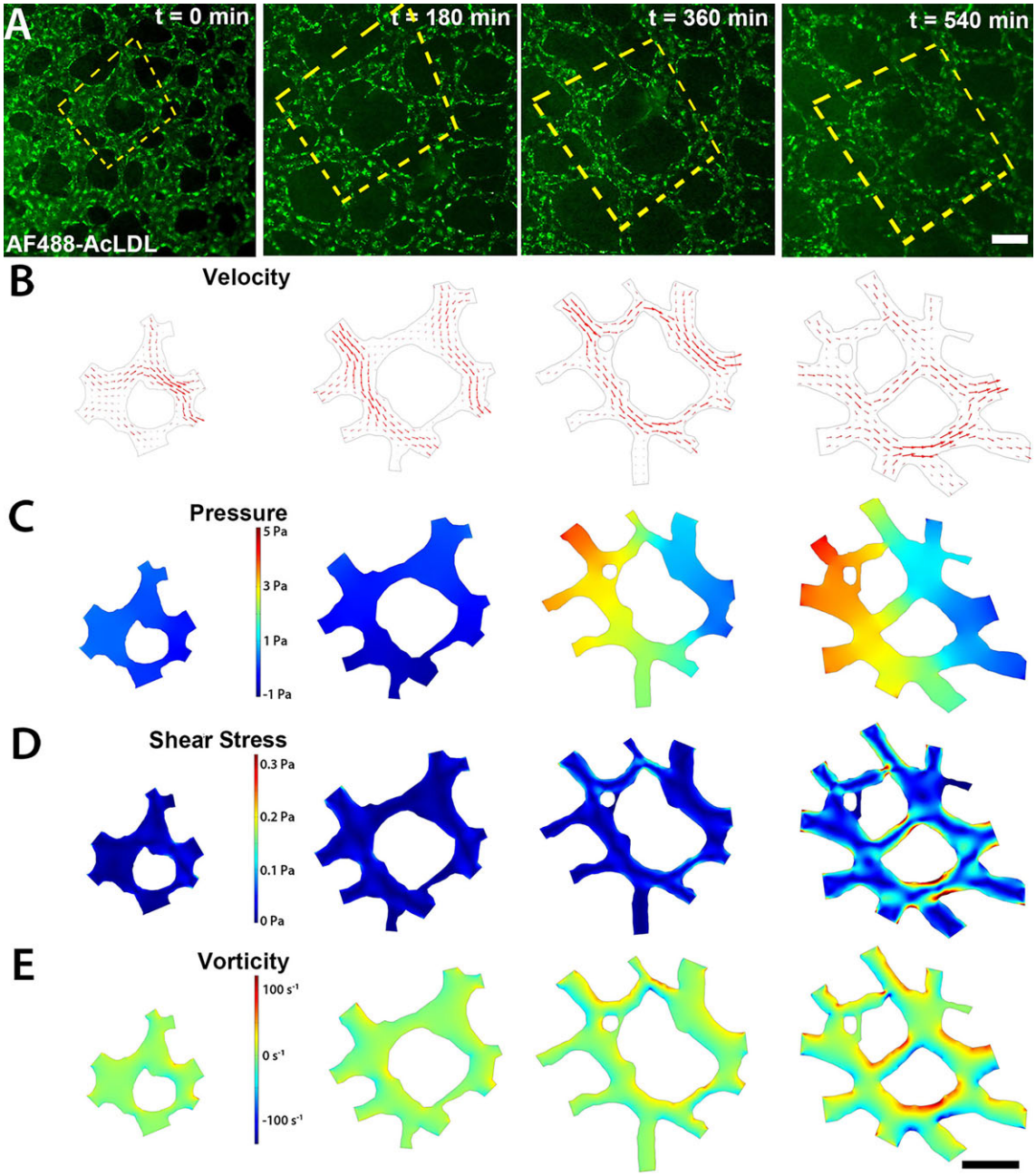

Fig. 4. Fluid dynamic analysis over a six-hour time-lapse period. Endothelial cells labelled with AF488-AcLDL and images were taken every 15 min for a period of 12-16 h. Full results from the time-lapse are available as Movies 1, 2 and 3. The embryo was at 13 somites or Hamburger Hamilton stage 11 at the start of the time-lapse experiment. The yellow box identifies the specific region that was analysed in this time-lapse (A). Flow was determined for the entire cardiac cycle, however only values for peak systole are presented. Blood flow velocities were analysed (B). The magnitude of the velocities is available in Movie 1. By combining viscosity estimates with the velocity profiles in the vessels, the pressure (C), shear stress (D) and vorticity (E) were calculated. Scale bars: 100 µm.

an older embryo (HH15), where we had observed flow reversal (Movie 4). This movie was taken with microspheres that had not been PEGylated, and therefore some clumps of microspheres were present. The clumps resulted in differences in the size of the particles that also allowed us to follow streamlines within the flow to ensure our CFD analysis was accurate. In this movie, the blood flow velocities from the inlet and the outlet on the left hand side of the image were entered into the CFD solver, and the outlet on the right hand side was set to a pressure value of zero. We found that our computational analysis accurately predicted the flow patterns observed, including the flow reversal, even though the input flow rates (i.e. the two left hand blood vessels) only exhibited forward flow without any reversal in the direction of flow. Furthermore, the streamlines predicted by the CFD analysis agreed with the experimental results.

To quantify the error associated with our method, we used the fact that one of our measured velocities was not used in the CFD analysis. We compared the measured value with the computed value at this last vessel segment (Fig. 5, Table 1). We also verified that the solution was not dependent on the mesh size chosen for the finite element grid by comparing the results for ‘fine’, ‘extra fine’ and ‘extremely fine’ mesh sizes. For all embryos, we analysed the error present during peak systolic flow. Decreasing the mesh size did not significantly change the computed velocities indicating mesh-

Development (2015) 142, 4158-4167 doi:10.1242/dev.127019

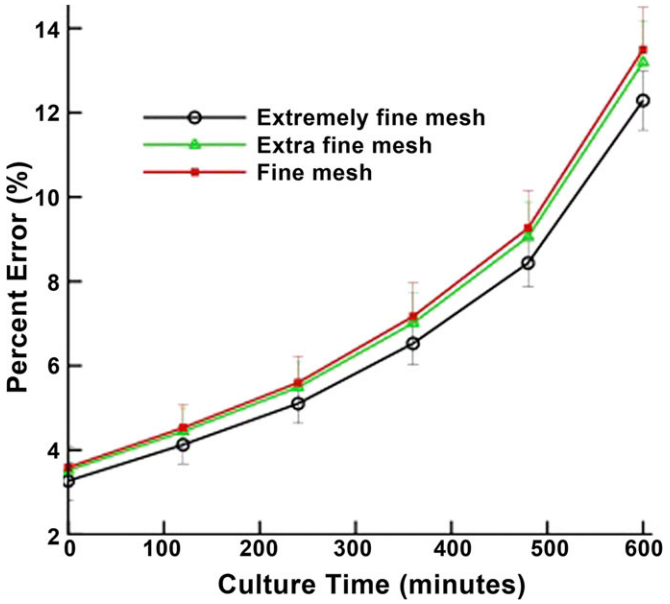

Fig. 5. Analysis of measurement error during time-lapse experiments. For a region of interest with *N* vessels entering or leaving the region, the blood velocities in *N–1* vessels were used in the computational analysis. For the last vessel, the outlet pressure was set to zero as a boundary condition. Error was calculated by comparing the calculated velocity for this last vessel with the measured value using μPIV. The error associated with the mesh size in the finite element analysis was investigated by using different settings for the mesh size in the CFD solver ('fine', 'extra fine' and 'extremely fine'). The percent error was very similar from one embryo to another, regardless of the magnitude of the velocity (Table 1). A trend of increasing error in the measurement was present as the time-lapse experiment progressed (n=9 embryos at each time point). Error bars represent standard deviation.

independence of the solution (Table 1). We performed error analysis on a total of 9 embryos that were followed by time-lapse microscopy. Interestingly, the error in the measurements changed very little from one embryo to another, even when a ten-fold difference in the velocity of the blood flow was present (compare Embryo 1 at 360 min to Embryo 2 at the same time point, Table 1). The error increased significantly as the time-lapse experiment proceeded, regardless of the mesh size used in the finite element model (Fig. 5). PEGylation reduces but does not abolish the adhesion of microspheres to the vessel wall. As the time-lapse progresses, the μPIV became less accurate as the number of particles in circulation decreased, resulting in an increased uncertainty in the measurements.

Studying the interaction of molecular and biomechanical stimuli

One of the strengths of this current technique is that we are able to study the interaction of protein signals and biomechanical signals. Therefore, as a first application of the technique, we studied the effect of shear stress on vessel enlargement and the effect of perturbing this process with a gain-of-function in TGFβ signalling. During vascular development, vessels that carry the most blood flow enlarge and those with the least flow regress (Thoma, 1893). Though this is a widely accepted concept, the relationship between the level of shear stress and changes in vessel diameter has never been investigated. We followed vessel diameter and shear stress in both enlarging (Fig. 6A) and regressing (Fig. 6B) vessels. We analysed a total of 3 embryos (at 16-19 time points), with 1-2 locations per embryo, for a total of 5 vessels. We plotted the percent change in vessel diameter between consecutive frames with respect to shear stress levels present and found that the natural logarithm of the shear stress correlates to the percent change in vessel diameter (Fig. 6C). From previous studies, we had observed that TGFβ injection during vascular remodelling in the embryo resulted in an increase in vessel diameters (unpublished observation). We therefore investigated whether TGFβ injection affected heart function and therefore altered shear stress levels, or whether the flow was unaltered but the response to shear stress was different. We injected embryos with TGFβ and analysed both changes in vessel diameter and shear stress levels (n=3 embryos, 7-9 time points per embryo, 1-2 locations per embryo, total of 5 vessels). The range of shear stress present in TGFβ-injected embryos did not differ from control embryos (P=0.726). When plotted on a semi-ln plot, however, a clear increase the rate at which vessels expanded for the same level of shear stress was present (Fig. 6D, P<0.0001). Though the intercept of the line was higher, the slope of the line was unchanged (P=0.926).

DISCUSSION

Hemodynamic signals are necessary for proper vascular development, however, the complexity of measuring shear stress levels in real time has hindered the study of the role of fluid forces in development. We previously showed that in unbranched vessels of the embryo, the velocity profile in the vessel is parabolic throughout the cardiac cycle (Jones et al., 2004). This occurs because two fluid dynamics parameters, the Reynold's number and the Womersley's number, are both very small for embryonic blood flow (i.e. less than one). It is because of these relatively simple flow dynamics that velocity, pressure drop and shear stress can accurately be calculated from the measured blood flow velocities. Though our results use

Table 1. Precise blood velocity values in *N–1* vessels of the measured and calculated velocity for three example embryos at two time points as represented in Fig. 5

		Embryo 1		Embryo 2		Embryo 3	
		No. elements	Velocity (μm/s)	No. elements	Velocity (μm/s)	No. elements	Velocity (μm/s)
t=0 min	μ-PIV	-	29.12	-	427.87	-	237.45
	Fine mesh	2106	28.04 (3.7)	3025	441.21 (3.1)	3381	227.45 (4.2)
	Extra fine mesh	2550	28.08 (3.6)	4763	440.87 (3.0)	5558	227.87 (4.0)
	Extremely fine mesh	4660	28.19 (3.2)	13186	440.49 (2.9)	17016	228.54 (3.8)
t=360 min	μ-PIV	-	325.13	-	2324.73	-	601.23
	Fine mesh	3608	300.34 (7.6)	9702	2479.67 (6.2)	3563	555.34 (7.6)
	Extra fine mesh	5477	301.21 (7.4)	17725	2477.97 (6.2)	6133	556.21 (7.5)
	Extremely fine mesh	13339	303.73 (6.6)	43355	2473.12 (6.0)	14940	559.12 (7.0)

Percentage error in parentheses. The error associated with the mesh size in the finite element analysis was investigated by using different settings for the mesh size in the CFD solver ('fine', 'extra fine' and 'extremely fine').

Development (2015) 142, 4158-4167 doi:10.1242/dev.127019

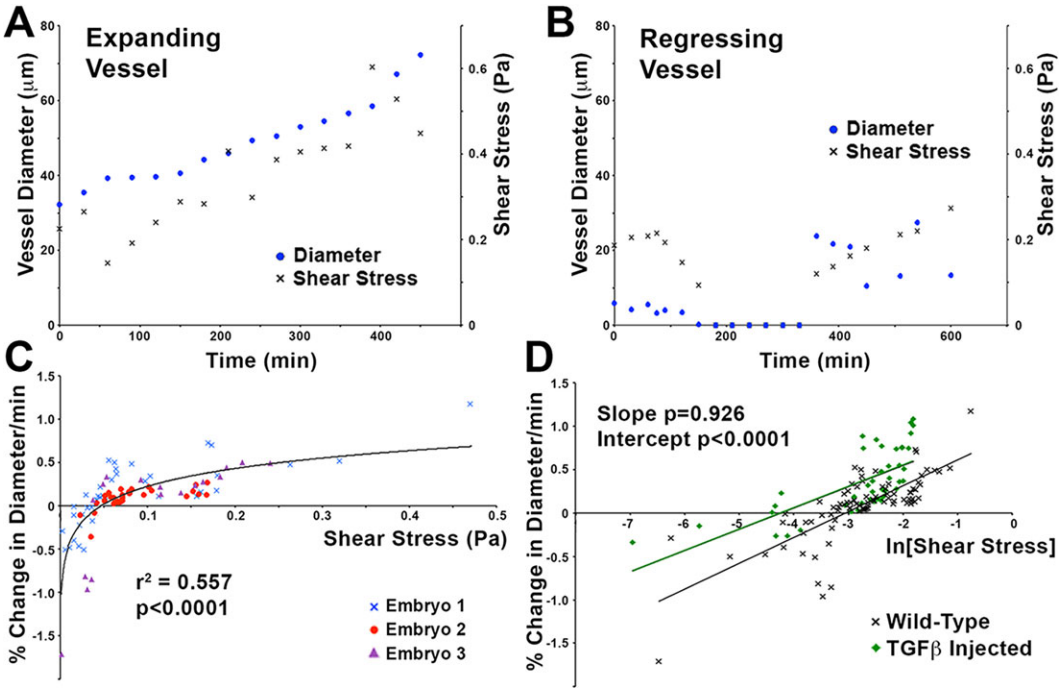

Fig. 6. Vessels enlarge and regress proportional to the logarithm of the shear stress. (A,B) The effect of shear stress on vessel diameter was studied by following both diameter (blue dots) and shear stress levels (black crosses) in enlarging (A) and regressing vessels (B). In the second example (B), the vessel regressed completely (150-330 min) before resprouting from the same location. (C) The percent change in vessel diameter per minute was proportional to the natural logarithm of the shear stress (P<0.0001). (D) TGFβ-injected embryos were analysed to investigate perturbed vessel enlargement. Injection of TGFβ did not affect the level of shear stress present (P=0.726) but did cause an increase in the rate of vessel enlargement. Data are plotted on a semi-ln plot. P-values were calculated using a two-tailed t-test.

embryos at the onset of blood flow, this technique can also be applied to embryos at older stages. Certain assumptions, however, such as the application of the Fahraeus relationship to calculate haematocrit, should be verified for older embryos before extending the technique to later stages.

One of the most significant limitations to the μPIV method is the adhesion of the tracer particles. Though PEGylation of the particles increased their time in circulation to ∼16 h, the errors associated with the velocity measurements increased as the time-lapse progressed. We chose to restrict our analysis to data from the first 10 h because of this limitation. Avian embryos can survive for 2-3 days in *ex ovo* culture, and we have found that the loss in AcLDL signal in the vessel wall over this period of time is not prohibitive. If the circulation time of the tracer particles could be further increased, it should be possible to extend this technique to follow vascular development and hemodynamics over a period of several days. We have tested particles with different surface charges, hydrophobicity and blocking reagents. None of these factors reduced the adhesion of particles to the vessel walls. PEGylation is currently the state-of-the-art for creating 'stealth' particles. We did not test different chain lengths, and small improvements on the time in circulation might be possible by optimising these factors.

The alternative to the use of tracer particles is to make flow measurements using techniques that do not require the use of tracers, such as Doppler OCT. Doppler OCT cannot produce images of the vascular network geometry at high enough resolution to accurately predict shear stress and pressure, but this could be resolved by combining Doppler OCT with confocal microscopy. The computational aspects of our current method could then be directly applied to such data sets. Combined OCT/confocal microscopy systems have previously been developed (Brinkmann et al., 2008; Podoleanu et al., 2004). The main disadvantage, however, is that such specialised and expensive equipment would limit the applicability of the method to labs that are specialised in this technique. Our μPIV-based method is therefore much more accessible to most groups. It requires only: (1) a micro-injector, (2) a fluorescent microscope, (3) a high-speed camera, and (4) a software license for a CFD solver. The cost of high-speed cameras has fallen drastically over the last decade. For any avian embryology lab, the cost of implementing this technique is reasonable.

Most fluid dynamic calculations do not include non-Newtonian properties of blood. Instead, a constant value of the viscosity based on the haematocrit is used. In large vessels, this approximation is justified, however, it is not appropriate for embryonic blood vessels. Embryonic blood flow is slow and shear-rate dependent effects are most pronounced at low shear rates. We were obliged, however, to extrapolate our previous viscosity data with respect to embryonic stage. Our previous results had shown that there was no change in apparent viscosity of blood with respect to stage when the haematocrit is below 50% (Al-Roubaie et al., 2011). Therefore, extrapolation results in similar values for the viscosity as using the data directly for the older embryos. Given that the embryonic vessels have haematocrits well below 20%, the assumption that stage has little effect on the viscosity is relatively safe. The inclusion of variation of the viscosity for haematocrit and shear rate in the flow calculation is a significant improvement on previous calculations of embryonic shear stress levels.

Our application of μPIV with CFD to investigate vessel enlargement found that vessels enlarge and regress proportional to the natural logarithm of the shear stress. This makes physiological sense, as there must be a maximum rate at which vessel can expand. We also found that injection of TGFβ causes an increase in the rate of vessel enlargement even though shear stress levels are

Development (2015) 142, 4158-4167 doi:10.1242/dev.127019

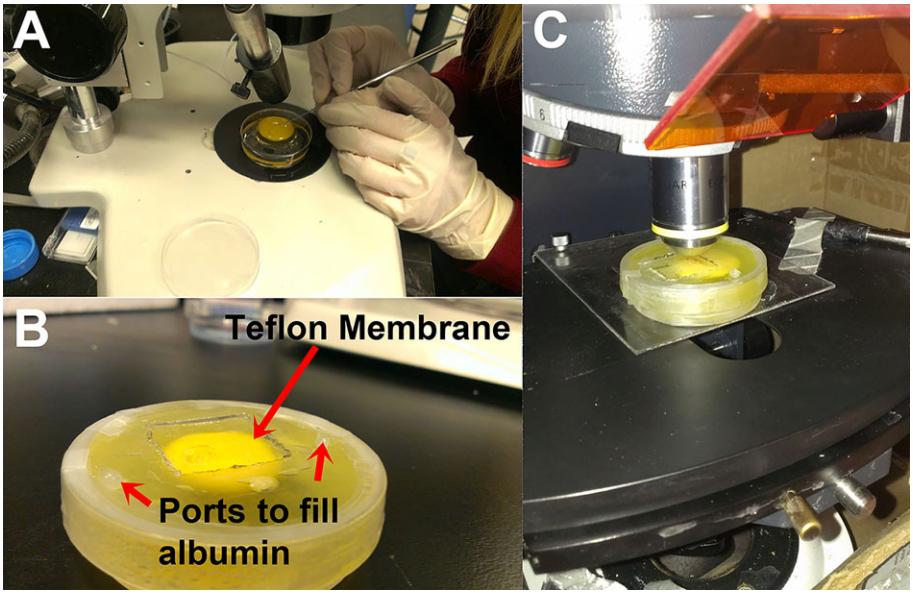

Fig. 7. Summary of embryo culture technique. Quail eggs were incubated until the appropriate stage and then transferred to a 6 cm Petri dish. (A) The embryos were injected with Alexa Fluor 488-acetylated low-density lipoprotein and red microspheres using a micro-injector. (B) The lid of the Petri dish was modified to create a Teflon window that is permeable to air but not to moisture. The lid was then sealed on the Petri dish using Parafilm. Additional warmed albumin was added to the dish, using small 'ports' located either side of the Teflon window. These were then sealed with vacuum grease. (C) The Petri dishes were transferred to a heated microscope stage. The vasculature was imaged every 15 min and the motion of the microspheres was imaged every 2 h.

unchanged. Interestingly, the injection affected the intercept but not the slope of the regression on a semi-ln plot. We are investigating agent-based simulations of cell movements to explain how a logarithmic relationship can arise between shear stress levels and vessel expansion or regression, as well as to examine which factors could be affected after TGFβ injection that would lead to the observed changes in behaviour. These results highlight the fact that neither molecular nor biomechanical stimuli should be studied in isolation. These signals interact, such that molecular signals affect how endothelial cells respond to blood flow, and vice versa.

This work represents the first technique to follow changes in flow dynamics as the vasculature remodels. It will allow for quantitative analysis of the relationships between hemodynamic parameters, such as shear stress and pressure drop, and biological processes in vascular remodelling. The resolution is high enough to investigate cellular mechanisms of remodelling in relationship to the flow. As such, this technique will allow investigators to begin to explore the interplay of flow dynamics and cellular events in vascular development.

MATERIALS AND METHODS

Simultaneous imaging of vascular remodelling and blood flow dynamics

All experimental methods were performed in accordance with the relevant guidelines on animal use. Fertilised quail eggs (*Coturnix japonica*) were incubated at 37°C until they reached a stage of 12-14 somites or HH11. Approximately 1 ml of albumin was removed from the egg by puncturing the shell with a syringe. A small window was cut into the top of the eggshell and the entire egg was poured into a 6 cm Petri dish, ensuring that the embryo remained on the top of the yolk (Fig. 7A). The embryos were injected intravascularly using a Picospritzer III micro-injector (Parker Hannifin) and a fine capillary glass needle with a tip diameter of ∼5 to 10 µm (Fig. 7A, Sutter Instruments, BF100-50-10). Alexa Fluor 488 acetylated low-density lipoprotein (AF488-AcLDL, Invitrogen, L-23380) was injected to label endothelial cells and FluoSpheres Carboxylate-Modified Microspheres FluoSpheres 0.5 µm, red fluorescent (580/605) (Invitrogen, F-8812) were injected as tracer particles to image the flow dynamics. Before injection, amino-PEG (Laysan Bio, MPEG-NH2-5000-1g) was covalently attached to the surface of the microspheres using a reduction reaction according to the manufacturer's instructions. Some minor modifications were made to the protocol. When washing the microspheres after the reduction reaction, an ultracentrifuge at 170,000 ***g*** was used instead of the recommended 25,000 ***g***. PEGylation made the particles much more neutrally buoyant such that the recommended centrifugation was ineffective. Furthermore, sodium azide was not added. A small amount of blue food dye (30% v/v) was added to all solutions to visualise the injection and ensure delivery specifically into the circulatory system. The volume of injection was titrated based on the volume of dye expunged (∼0.1 µl injected per embryo). Before and after injection, embryos were rehydrated with Ringer's solution. Only embryos where the injection was specific to the vasculature on the first attempt were kept for time-lapse imaging. In general, a dozen embryos were injected and the most successful injection, assessed on the fluorescent microscope, was used for each experiment. Embryo culture for time-lapse microscopy was done as previously described (Al-Roubaie et al., 2012). A large square hole was made in the lid of the Petri dish (∼2 cm×2 cm), as well as two smaller 'ports' about the size of a syringe needle (Fig. 7B). The square hole was covered with a Teflon membrane, which is permeable to air and not to moisture (YSI, 066156). The Teflon membrane was affixed using silicon vacuum grease (Dow Corning, 1597418). The lid was sealed onto the Petri dish using Parafilm. The Petri dish was then filled with additional warmed albumin through the 'ports' until the embryo was in direct contact with the Teflon membrane. The ports were plugged with silicon vacuum grease (Fig. 7B). Embryos were imaged on an upright fluorescence microscope equipped with an Axiocam MRC for images of the vascular morphology and a high-speed camera (Photron FASTCAM Ultima APX-RS) for images of the microsphere motion (Fig. 7C). A homemade heater box was built around the microscope stage to keep the microscope stage at 37°C, using a small room heater and a temperature controller (VWR, 10171-512). Endothelial cells were imaged every 15 min. Blood flow dynamics were imaged at 250 fps for 2 full cardiac cycles (equivalent to 2 s of imaging time), once every 2 h.

Creation of an image mask

A MATLAB program (R2014b, Mathworks) was developed in Simulink for the post-processing of acquired images. At each time point, the green image (endothelial cells) and the stack of 500 red images (microsphere motion) were flattened into a single image. The flattened image was converted to a grey-scale image. A gamma correction was applied to control the overall brightness of the image and the contrast was adjusted by linearly scaling the pixel values (see Fig. S1 for the Simulink block diagram). The gamma parameter and the break point of the straight line segment were altered manually to obtain the best possible contrast. The illumination was equalised using histogram equalisation. To reduce noise, a median filter was applied to the image, and then the image was thresholded to obtain a binary image used as a 'mask'. The image mask was used to subtract all background noise and make non-flow regions into pure black. It was applied to each individual frame of the microsphere motion before µPIV analysis.

Development (2015) 142, 4158-4167 doi:10.1242/dev.127019

Identification of walls, centreline and local vessel radius

To identify the inner wall boundaries of perfused vessels, Matlab's 'edge' function was applied to the image mask, specifying a Canny algorithm. The Canny edge detector creates a rough estimate of every possible edge contour within the image; the edge information was saved to a binary edge detected map. As there were still some discontinuous edges in the image, edge points were linked to nearby edges using an edge connection algorithm based on a least squares method to create a closed, continuous boundary (Hoover and Goldbaum, 2003). The centreline of each vessel was found by skeletonising the image mask. Using a search-based method within MATLAB, the distance between the centreline and the closest black pixel of the edge map was measured to define the local radius of vessel.

Micro-particle image velocimetry analysis

Micro-PIV was used to measure velocity waveforms during the cardiac cycle at inlets and outlets. A pair of images was divided into smaller areas called interrogation windows. These interrogation windows were compared in two consecutive images using a MATLAB code to seek the most likely position of these windows from one frame to other one. The velocity of the particles can be obtained by calculating the distance between the centres of these two interrogation windows. Therefore the local velocity vector is:

$$\vec{v}(x,\ y,\ t) = \frac{\Delta x(x,\ y,\ t)}{\Delta t}. \qquad (3)$$

In this equation, Δx denotes the displacement of the cluster after a time interval Δt of between two consecutive frames. An interrogation window size of 16×16 pixels was used. Flow inlets and outlets were chosen far from branch points. As the Reynolds number for the flow is very close to one and the Womersley number is less than one (Jones et al., 2004), entrance length effects are on the order of one micron, hence a fully developed parabolic velocity profile was assumed for the μPIV analysis.

Blood rheology

A relationship between haematocrit and embryonic stage was obtained by injecting FITC-dextran (Sigma-Aldrich, FD40S) into quail embryos. Line scans on live embryos were performed on a heated confocal microscope stage as previously described (Jones et al., 2004). Several images were obtained at different embryonic stages and vessel diameters. Images were thresholded to obtain the tube haematocrit and the vessel diameter was measured. For smaller vessels (tube diameter less than 300 μm), the haematocrit was adjusted for tube diameter based on the Fahraeus equation (Pries et al., 1990). A relationship between the discharge haematocrit and embryonic stage was developed (Fig. 2). A cubic fit was used as a method to interpolate between stages in the computational model. Blood viscosity was calculated based on embryonic stage and vessel diameter, using a Carreau relationship that we previously developed to describe the non-Newtonian behaviour of embryonic blood flow (Al-Roubaie et al., 2011). The constants were re-evaluated from the paper to include a larger number of haematocrit values. We interpolated (for haematocrit) and extrapolated (for embryonic stage) to establish the value of the constants (μ_∞, μ_0, λ and n) for the time-lapse experiments.

Computational fluid dynamics

The vascular geometry obtained by image processing and the inlet and outlet velocities acquired by μPIV were imported into a CFD solver (COMSOL Multiphysics). The governing equations inside the vessels (i.e. continuity and momentum equations for laminar, unsteady, non-Newtonian, incompressible flow) were solved using a finite elements method. From N inlets and outlets, the flow rates at $N-1$ points were set as boundary conditions. For the last outlet, a straight section of vessel was added to allow the flow to reach fully developed conditions and help the convergence of the numerical solution inside the domain. The fully developed boundary condition was applied at the extended outlet of the domain (depends on Reynolds number), i.e. $\frac{\partial}{\partial_x} = 0$. Vessel walls were assumed to be rigid and impermeable with no slip boundary conditions. The rigid wall assumption was confirmed using high-speed images of the vessel wall (Movie 5). As the domain has curved geometries, the numerical algorithm was applied on a non-orthogonal curvilinear coordinate framework. Mesh generation and solution was performed with COMSOL. The domain was meshed with extremely fine free triangular meshes. Numerical simulations were conducted using a computer equipped with two Quad Core Intel(R) Processors (8 nodes each 3.40 GHz).

Acknowledgements

We thank Espen Jahnsen for insightful discussion and assistance in the production of time-lapse recordings.

Competing interests

The authors declare no competing or financial interests.

Author contributions

S.G. designed experiments, performed experiments, developed the computational algorithms, analysed the results and wrote the manuscript. R.L.L. developed the computational algorithms, analysed results and wrote the manuscript. E.A.V.J. designed experiments, performed experiments, analysed the results and wrote the manuscript.

Funding

E.A.V.J. was supported by grants from the Sick Kids Foundation of Canada [NI12-029] and a grant from Life Science Research Partners. R.L.L. was supported by grants from Canadian Institute of Health Research [MOP-119292]. A McGill Engineering Doctoral Award supported S.G.

Supplementary information

Supplementary information available online at
http://dev.biologists.org/lookup/suppl/doi:10.1242/dev.127019/-/DC1

References

Abe, J.-i. and Berk, B. C. (2014). Novel mechanisms of endothelial mechanotransduction. *Arterioscler. Thromb. Vasc. Biol.* **34**, 2378-2386.

Adrian, R. J. (1991). Particle-imaging techniques for experimental fluid mechanics. *Annu. Rev. Fluid Mech.* **23**, 261-304.

Al-Roubaie, S., Jahnsen, E. D., Mohammed, M., Henderson-Toth, C. and Jones, E. A. V. (2011). Rheology of embryonic avian blood. *Am. J. Physiol. Heart Circ. Physiol.* **301**, H2473-H2481.

Al-Roubaie, S., Hughes, J. H., Filla, M. B., Lansford, R., Lehoux, S. and Jones, E. A. V. (2012). Time-lapse microscopy of macrophages during embryonic vascular development. *Dev. Dyn.* **241**, 1423-1431.

Brinkmann, C. K., Wolf, S. and Wolf-Schnurrbusch, U. E. K. (2008). Multimodal imaging in macular diagnostics: combined OCT-SLO improves therapeutical monitoring. *Graefes Arch. Clin. Exp. Ophthalmol.* **246**, 9-16.

Bryan, M. T., Duckles, H., Feng, S., Hsiao, S. T., Kim, H. R., Serbanovic-Canic, J. and Evans, P. C. (2014). Mechanoresponsive networks controlling vascular inflammation. *Arterioscler. Thromb. Vasc. Biol.* **34**, 2199-2205.

Canny, J. (1986). A computational approach to edge detection. *IEEE Trans. Pattern Anal. Mach. Intell.* **PAMI-8**, 679-698.

Chapman, W. B. (1918). The effect of the heart-beat upon the development of the vascular system in the chick. *Am. J. Anat.* **23**, 175-203.

Chouinard-Pelletier, G., Jahnsen, E. D. and Jones, E. A. V. (2013). Increased shear stress inhibits angiogenesis in veins and not arteries during vascular development. *Angiogenesis* **16**, 71-83.

Fahraeus, R. (1929). The suspension stability of the blood. *Physiol. Rev.* **9**, 241-274.

Gijsen, F. J. H., Wentzel, J. J., Thury, A., Lamers, B., Schuurbiers, J. C. H., Serruys, P. W. and van der Steen, A. F. (2007). A new imaging technique to study 3-D plaque and shear stress distribution in human coronary artery bifurcations in vivo. *J. Biomech.* **40**, 2349-2357.

Hoover, A. and Goldbaum, M. (2003). Locating the optic nerve in a retinal image using the fuzzy convergence of the blood vessels. *IEEE Trans. Med. Imaging* **22**, 951-958.

Immordino, M. L., Dosio, F. and Cattel, L. (2006). Stealth liposomes: review of the basic science, rationale, and clinical applications, existing and potential. *Int. J. Nanomedicine* **1**, 297-315.

Jones, E. A. V. (2011). Mechanical factors in the development of the vascular bed. *Respir. Physiol. Neurobiol.* **178**, 59-65.

Jones, E. A. V., Baron, M. H., Fraser, S. E. and Dickinson, M. E. (2004). Measuring hemodynamic changes during mammalian development. *Am. J. Physiol. Heart Circ. Physiol.* **287**, H1561-H1569.

Lucitti, J. L., Jones, E. A. V., Huang, C., Chen, J., Fraser, S. E. and Dickinson, M. E. (2007). Vascular remodeling of the mouse yolk sac requires hemodynamic force. *Development* **134**, 3317-3326.

Development (2015) 142, 4158-4167 doi:10.1242/dev.127019

Manbachi, A., Hoi, Y., Wasserman, B. A., Lakatta, E. G. and Steinman, D. A. (2011). On the shape of the common carotid artery with implications for blood velocity profiles. *Physiol. Meas.* **32**, 1885-1897.

Mantha, A., Karmonik, C., Benndorf, G., Strother, C. and Metcalfe, R. (2006). Hemodynamics in a cerebral artery before and after the formation of an aneurysm. *Am. J. Neuroradiol.* **27**, 1113-1118.

Meinhart, C. D., Wereley, S. T. and Gray, M. H. B. (2000). Volume illumination for two-dimensional particle image velocimetry. *Meas. Sci. Technol.* **11**, 809-814.

Milkiewicz, M., Brown, M. D., Egginton, S. and Hudlicka, O. (2001). Association between shear stress, angiogenesis, and VEGF in skeletal muscles in vivo. *Microcirculation* **8**, 229-241.

Pitts, K. L., Mehri, R., Mavriplis, C. and Fenech, M. (2012). Micro-particle image velocimetry measurement of blood flow: validation and analysis of data pre-processing and processing methods. *Meas. Sci. Technol.* **23**, 105302.

Podoleanu, A. G., Dobre, G. M., Cucu, R. G. and Rosen, R. B. (2004). Sequential optical coherence tomography and confocal imaging. *Opt. Lett.* **29**, 364-366.

Poelma, C., Vennemann, P., Lindken, R. and Westerweel, J. (2008). In vivo blood flow and wall shear stress measurements in the vitelline network. *Exp. Fluids* **45**, 703-713.

Pries, A. R., Secomb, T. W., Gaehtgens, P. and Gross, J. F. (1990). Blood flow in microvascular networks. Experiments and simulation. *Circ. Res.* **67**, 826-834.

Robles, L. Y., Singh, S. and Fisichella, P. M. (2015). Emerging enhanced imaging technologies of the esophagus: spectroscopy, confocal laser endomicroscopy, and optical coherence tomography. *J. Surg. Res.* **195**, 502-514.

Santiago, J. G., Wereley, S. T., Meinhart, C. D., Beebe, D. J. and Adrian, R. J. (1998). A particle image velocimetry system for microfluidics. *Exp. Fluids* **25**, 316-319.

Steinman, D. A., Milner, J. S., Norley, C. J., Lownie, S. P. and Holdsworth, D. W. (2003). Image-based computational simulation of flow dynamics in a giant intracranial aneurysm. *Am. J. Neuroradiol.* **24**, 559-566.

Thoma, R. (1893). *Untersuchungen über die Histogenese und Histo- mechanik des Gefäßsystems*. Stuttgart, Germany: Ferdinand Enke.

Wakimoto, K., Kobayashi, K., Kuro, O. M., Yao, A., Iwamoto, T., Yanaka, N., Kita, S., Nishida, A., Azuma, S., Toyoda, Y. et al. (2000). Targeted disruption of Na+/Ca2+ exchanger gene leads to cardiomyocyte apoptosis and defects in heartbeat. *J. Biol. Chem.* **275**, 36991-36998.

Ziada, A., Hudlicka, O. and Tyler, K. R. (1989). The effect of long-term administration of alpha-1-blocker prazosin on capillary density in cardiac and skeletal muscle. *Pflugers Arch. Eur. J. Physiol.* **415**, 355-360.